Check for updates

CONDENSED MATTER PHYSICS

Interaction-driven flat band and charge order in Fe_5GeTe_2

Qiang Gao[1]†, Gabriele Berruto[1]†, Khanh Duy Nguyen[1], Chaowei Hu[2], Paul Malinowski[2], Haoran Lin[1], Beomjoon Goh[3], Bo Gyu Jang[4], Xiaodong Xu[2], Peter Littlewood[5,6], Jiun-Haw Chu[2], Shuolong Yang[1]*

Copyright © 2026 The Authors, some rights reserved; exclusive licensee American Association for the Advancement of Science. No claim to original U.S. Government Works. Distributed under a Creative Commons Attribution NonCommercial License 4.0 (CC BY-NC).

Flat electronic bands enable fascinating emergent phenomena such as superconductivity and charge orders. A prevailing approach to realizing flat bands is to engineer lattice geometric constraints in twisted or kagome-like materials. An alternative approach is to utilize purely electronic-interaction-driven flat bands, yet a fundamental challenge is that extreme flatness requires ultrastrong interaction strength, which often leads to incoherent states. Here we demonstrate the concurrent formation of an interaction-driven flat band at the Fermi level and a $\sqrt{3} \times \sqrt{3}R30°$ charge order in a van der Waals magnet Fe_5GeTe_2 using high-resolution angle-resolved photoemission spectroscopy. This charge order is manifested by band folding within 30 meV below the Fermi level, with its nesting driven by flat bands. The presence of this flat band throughout the Brillouin zone and the logarithmic temperature dependence of its spectral weight suggest a phenomenological Kondo-like, coherent Fermi liquid emerging from strong correlations. Our work establishes a paradigm where an interaction-driven flat band promotes large-scale electronic ordering.

INTRODUCTION

Flat electronic bands in solid-state systems can fundamentally reshape the collective ground states and lead to fascinating orders such as charge orders (*1*), superconductivity (*2*, *3*), correlated insulators (*4*), as well as integer (*5*) and fractional topological orders (*6*–*8*). Flat bands can be obtained by engineering lattice geometric constraints, most notably via moiré potentials in twisted 2D materials and via destructive quantum interference in special lattices. Yet, in twisted 2D materials, the flat-band condition is often unstable against sample handling, and the uniformity of the moiré pattern is restricted to <1 μm. In lattices with special geometries, such as Lieb (*9*, *10*), kagome (*11*–*15*), and clover (*16*) lattices, the flat bands are often hundreds of meV away from the Fermi level (E_F), making them irrelevant for low-energy ordering phenomena. Moreover, such flat bands are fully determined by the crystal structures and exhibit minimum tunability. Therefore, there has been a growing interest in finding alternative flat-band systems that are robust, tunable, and extendable to large spatial scales, ideal for investigating the interplay of electron correlations, topology, and charge orders at E_F (*17*, *18*).

Electronic-interaction-driven flat bands provide a different possibility. Strong electron-electron, electron-phonon, or electron-spin interactions lead to band structure renormalization close to E_F (*19*). In fact, in some twisted 2D materials (*20*) or geometrically constrained lattices (*21*), electronic interactions have been shown to contribute substantially to band flattening. It is thus inspiring to explore purely interaction-driven flat bands for emergent quantum phenomena. Such band flattening can be robust against sample handling, tunable by carrier doping or temperature variation, and extendable to macroscopic length scales. It can provide an avenue to induce and tune charge orders or charge density waves, which have been prevalent in transition metal dichalcogenides and kagome-like materials (*22*–*28*). However, a fundamental challenge is that extreme band flatness often requires a diverging interaction strength, which in turn can lead to incoherent states. Such incoherent interaction-driven flat bands (*29*) cannot be utilized to enable emergent orders near E_F.

Here we focus on Fe_5GeTe_2 which is a van der Waals magnetic material holding an exciting potential for flat-band engineering. Fe_5GeTe_2 has multiple structural phases distinguished by the ordering of the Fe (1) atoms, which can occupy one of the up and down sites relative to the Ge atom in each unit cell (*30*–*35*). In the so-called site-ordered phase, the Fe (1) atoms follow an "up-down-down" or "down-up-up" (UDD or DUU) arrangement to form a clover lattice (Fig. 1B), where flat bands away from E_F emerge due to destructive quantum interference. Meanwhile, theory predicted that an effective Kondo-like interaction between the flat bands and the dispersive conduction bands in a clover lattice leads to new flat bands exactly at E_F (*16*). A recent scanning tunneling microscopy (STM) study (*36*) revealed that flat bands appear concomitantly with a $\sqrt{3} \times \sqrt{3}R30°$ charge order in the "UUU" phase of Fe_5GeTe_2. The crucial difference between this charge order and the structural $\sqrt{3} \times \sqrt{3}$ order in the UDD or DUU phase is that the former does not exhibit the lattice reconstruction and is purely electronically driven. However, so far flat bands at E_F associated with either the electronic or structural $\sqrt{3} \times \sqrt{3}$ order in Fe_5GeTe_2 have not been clearly revealed using angle-resolved photoemission spectroscopy (ARPES) (*35*, *37*–*40*), making it difficult to investigate how flat bands impact electronic orders in this van der Waals magnet. We note that recent studies on Fe_5GeTe_2 in the slow-cooled phase (*41*, *42*) reported flat bands close to E_F, yet no Fermi surface reconstruction due to a $\sqrt{3} \times \sqrt{3}$ order has been reported, making it not suitable for studying the interplay between flat bands and charge orders.

[1]Pritzker School of Molecular Engineering, The University of Chicago, Chicago, Illinois 60637, USA. [2]Department of Physics, University of Washington, Seattle, Washington 98195, USA. [3]Department of Physics and Astronomy, Seoul National University, Seoul 08826, Republic of Korea. [4]Department of Advanced Materials Engineering for Information and Electronics, Kyung Hee University, Yongin 17104, Republic of Korea. [5]James Franck Institute and Department of Physics, The University of Chicago, Chicago, Illinois 60637, USA. [6]School of Physics and Astronomy, University of St Andrews, N Haugh, St Andrews KY16 9SS, United Kingdom.
*Corresponding author. Email: yangsl@uchicago.edu
†These authors contributed equally to this work.

Downloaded from https://www.science.org on October 20, 2026

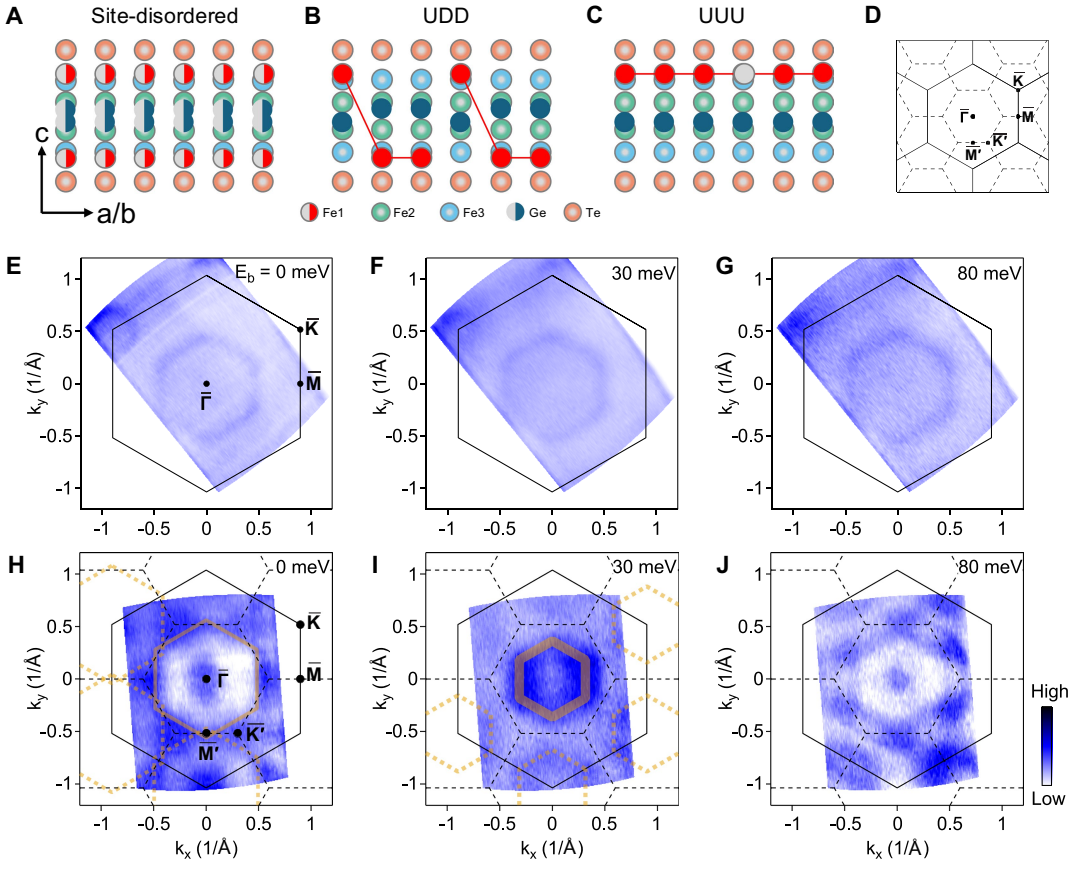


Fig. 1. Distinct phases in Fe_5GeTe_2. (**A** to **C**) Schematic crystal structures of different Fe_5GeTe_2 phases, projected along the [120] direction. The Fe (1) atoms, shown as red spheres, can occupy two split-site positions-either above or below the Ge atom-referred to as the U (up) and D (down) sites, respectively. In the site-disordered phase (A), the Fe (1) atoms randomly occupy the U and D sites. In the UDD phase (B), Fe (1) atoms form an ordered superstructure with a periodic U-D-D arrangement. In the UUU phase (C), all Fe (1) atoms occupy the U sites. Half-filled circles indicate a 50% occupancy probability, and empty circles indicate vacancies. (**D**) Brillouin zone schematics: black solid lines show the original Brillouin zone, and black dashed lines show the reconstructed $\sqrt{3} \times \sqrt{3}$ Brillouin zone. (**E** to **G**) Fermi surface map (E) and constant energy contours at binding energies of 30 meV (F) and 80 meV (G) for the UDD phase. (**H** to **J**) Same as (E to G), but measured for the UUU phase. All data in this figure were measured at 8 K using unpolarized 21.2 eV photons.

In this article, we report the discovery of a $\sqrt{3} \times \sqrt{3}R30°$ charge order driven by flat bands at E_F in Fe_5GeTe_2. Multiple phases are identified by high-resolution ARPES. In one phase unrevealed by previous ARPES studies, electronic structures are folded to the $\sqrt{3} \times \sqrt{3}$ reconstructed Brillouin zone, yet the band folding is limited to a small binding energy range less than 30 meV, indicating the purely electronic origin of this order. The nesting vector connects segments of the Fermi surfaces where the flat band is pronounced in the ARPES spectrum. The characteristics of the flat band, that it is omnipresent throughout the Brillouin zone and exhibits a logarithmically growing spectral weight towards lower temperatures, point to a phenomenological Kondo-like, coherent Fermi liquid emerging from strong correlation physics. Taken together with the calculation of Lindhard response functions for both the dispersive-band and flat-band regimes, we conclude that the flat band dramatically enhances the tendency for Fermi surface nesting. This makes Fe_5GeTe_2 a unique non-twisting system to demonstrate the generalizable scheme where interaction-driven flat bands at E_F lead to electronic ordering.

RESULTS

The electronic structures of two distinct phases of Fe_5GeTe_2 are revealed by ARPES using 21.2 eV photons (Fig. 1). Importantly, we use 6 eV laser-based micrometer-scale ARPES to visualize the microscopic mixture of different phases (fig. S1). This enables us to select the material allowing helium-lamp-based ARPES at 21.2 eV with a 0.5 mm beam spot to investigate regions dominated by a single phase. By rapidly quenching the sample from 550 K to 273 K we preferentially obtain Phase I (Fig. 1, E to G). Here, a hexagonal hole pocket and a quasi-circular electron pocket are observed at the $\overline{\Gamma}$ and $\overline{K}$ points of the unreconstructed Brillouin zone. These observations are generally consistent with those in the previously revealed site-ordered phase (*35*). Moreover, a geometrically induced flat band at −0.5 eV is observed in this phase (fig. S2), reinforcing the assignment to the site-ordered phase (*35*). Consistent with the prior study on the site-ordered phase (*35*), we also do not observe band folding in this phase, possibly due to the short coherence length of each "UDD" or "DUU" domain (*36*). By slowly cooling the sample from 550 K to 300 K with a 2–4 K/min cooling rate we have a higher probability of

Downloaded from https://www.science.org on October 20, 2026

observing Phase II, where diffusive features are observed at the $\overline{\Gamma}$ and $\overline{K}$ points in the Fermi surface map (Fig. 1H). Six triangular features are resolved at the 6 corners of the reconstructed Brillouin zone. The Fermi surface topology is consistent with a $\sqrt{3} \times \sqrt{3}$ reconstructed Brillouin zone. The rather diffusive features in the Fermi surface map reflect flat band dispersions in the energy-momentum cuts (Fig. 2D). We also reveal a more subtle band folding at the binding energy of 30 meV (Fig. 1I), where the original hexagonal contour at $\overline{\Gamma}$ leads to folded replicas at the 6 $\overline{K}$ points. The low-energy electronic ordering is also manifested in the replication of the band dispersions at $\overline{\Gamma}$ and $\overline{K}$ (Fig. 2C). Finally, we do not observe band folding at the binding energy of 80 meV (Fig. 1J). The confined energy range for band folding is inconsistent with a lattice-based $\sqrt{3} \times \sqrt{3}$ order, indicating that the charge order in Phase II is likely electronically driven.

A flat band at E_F is observed in the charge-ordered Phase II. This is seen by plotting the energy-momentum cuts along the high-symmetry trajectories in the momentum space (Fig. 2B). Figure 2D shows that the Fermi surface feature at $\overline{\Gamma}$ and the triangular features at the folded zone corners $\overline{K'}$ are related to flat band dispersions (α). To better visualize the α band, the energy-momentum spectra (Fig. 2, D, F, and G) are divided by the Fermi-Dirac function convolved with the energy resolution. Raw spectra are plotted in fig. S4. The energy distribution curves (EDCs) taken around $\overline{\Gamma}$ and $\overline{K'}$ exhibit a pronounced peak which is relatively momentum-independent and pinned at E_F (Fig. 2E), demonstrating a non-dispersive band at E_F. In addition, a weakly-dispersive, electron-like band (β) at 30 meV below E_F is observed by both 21.2 eV (Fig. 2D) and 6 eV photons with a *p*-polarization (Fig. 2F). *S*-polarized 6 eV light preferentially enhances the α band over a broader momentum range (Fig. 2, G and H). Figure 2G also suggests that the α feature connects to a dispersive hole-like band at momenta beyond [−0.2, 0.2] $Å^{-1}$. The *p*- and *s*-polarized light yield stronger cross-sections on the right and left part of the electronic structure, respectively. A more detailed study suggests that the linear dichroism follows the C_3 symmetry (fig. S5), as expected for the rhombohedral stacking of Fe_5GeTe_2 slabs (*30*). In a traditional electronically driven charge-density wave, the tendency for nesting is the strongest when there is a nesting vector connecting parallel segments of the Fermi surface

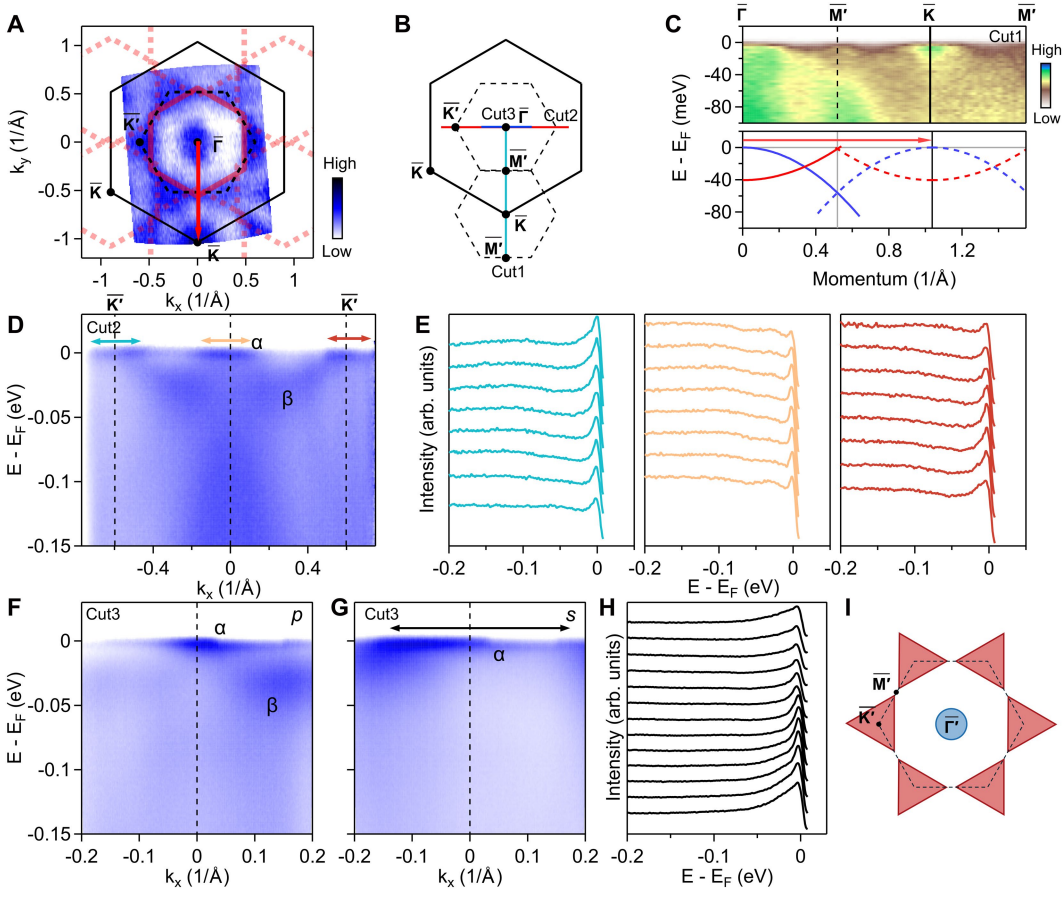


Fig. 2. Charge order and flat band in the UUU phase of Fe_5GeTe_2. (**A**) Fermi surface map. (**B**) Brillouin zone schematics: solid hexagon indicates the original Brillouin zone, and the dashed hexagons represent the reconstructed $\sqrt{3} \times \sqrt{3}$ Brillouin zone. (**C** to **D**) High-symmetry momentum cuts, with cut directions indicated in (B). In (C), the blue and red curves mark the electron and hole bands near $\overline{\Gamma}$, while dashed curves mark their replica bands folded to $\overline{K}$ due to the $\sqrt{3} \times \sqrt{3}$ reconstruction. (**E**) Momentum-dependent energy-distribution curves (EDCs) taken at equally spaced momentum points in D. (**F** to **G**) Dispersions along Cut3 measured with 6-eV laser in *p* (F) and *s* (G) polarizations. (**H**) EDCs taken from (G), emphasizing the flat band at the Fermi level. (**I**) Schematic of the reconstructed Fermi surface in the reconstructed Brillouin zone. The blue circle near $\overline{\Gamma'}$ corresponds to the flat band connected to a hole-like band, while red triangles near $\overline{K'}$ indicate flat bands connected to an electron-like band (fig. S6). Data in (D to H) are divided by the Fermi-Dirac function convolved with the energy resolution.

Downloaded from https://www.science.org on October 20, 2026

(*43*). However, such a nesting vector defined by the hexagonal pocket (solid red in Fig. 2A) is along $\overline{\Gamma}-\overline{M}$, inconsistent with the folding between $\overline{\Gamma}$ and $\overline{K}$. Instead, the nesting vector directly connecting $\overline{\Gamma}$ and $\overline{K}$ links the momentum-space segments where the flat band feature α is pronounced. We will show in the Discussion section that such a flat band configuration dramatically promotes electronic ordering. Moreover, Fig. 2, D and F illustrate that flat dispersions are seen both at 0 and 30 meV below E_F, which explains the fact that band folding at these energies is detectable, as shown in Fig. 1, H and I.

We discuss the possible structural origin of Phase II. Importantly, structural phase assignments of Fe_5GeTe_2 in the ARPES literature (*35*, *37*–*42*) have been particularly controversial due to the multiple possible structural configurations overlooked by early ARPES studies. Even though some studies (*38*, *40*) claimed to have observed band folding between $\overline{\Gamma}$ and $\overline{K}$, the replication of the Fermi surfaces was not clearly resolved. The folded band observed in Ref. (*38*) extends to 200 meV below E_F, with no concomitant flat bands near E_F, indicating a structural origin different from our Phase II. Later ARPES studies (*35*, *39*, *41*, *42*) discovered multiple structural configurations leading to distinct electronic structures. Wu *et al.* (*35*, *41*) identified the electronic structures for the site-ordered phase obtained by rapid thermal quenching, and the site-disordered phase by slow cooling. Huang *et al.* (*39*) assigned two types of electronic structures to the Fe (1) and Fe (5) terminations. Our Phase I exhibits an electronic structure that mimics both the site-ordered phase in Wu *et al.* and the Fe (5) termination in Huang *et al.*: dispersive hole pockets near $\overline{\Gamma}$ and a small electron pocket near $\overline{K}$. Here we mainly follow the phase assignments in Ref. (*35*) considering its explicit investigation of the lattice symmetry using optical second harmonic generation. While it is tempting to attribute our Phase II to the site-disordered phase according to the thermal trajectory, Phase II exhibits a markedly different electronic structure. The site-disordered phase features multiple dispersive hole pockets near $\overline{\Gamma}$ and dispersive electron pockets near $\overline{K}$. Neither the $\sqrt{3}\times\sqrt{3}$ Fermi surface reconstruction nor the pronounced flat band at E_F below 100 K was observed in the site-disordered phase (*35*). Moreover, we utilized 6 eV laser-based micro-ARPES and discovered two kinds of electronic structures different from that of the site-ordered phase (fig. S3). One corresponds to Phase II where diffusive Fermi surface features appear at $\overline{\Gamma}$ and $\overline{K}$ associated with flat band dispersions (Fig. 2A). The other (Phase III) shows dispersive hole bands near $\overline{\Gamma}$ but no strong feature at −0.5 eV. The feature at −0.5 eV is a signature of the site-ordered phase (fig. S1B). This comparison suggests that Phase III is more consistent with the characteristics of the site-disordered phase, but Phase II is yet a different phase. We point out that there is a strong similarity between the flat band observed in our Phase II and that in the slow-cooled phase in Huh *et al.* (*42*), yet the $\sqrt{3}\times\sqrt{3}$ Fermi surface reconstruction was missing in Ref. (*42*), possibly due to sample quality or photon-energy-dependent matrix element effects. Considering the observation of the $\sqrt{3}\times\sqrt{3}$ Fermi surface reconstruction and that of the flat bands, we conclude that the most likely scenario is that Phase II corresponds to the charge-ordered state identified with the "UUU" configuration in a previous STM study (*36*).

We proceed to reveal the nature of the flat band at E_F by conducting temperature-dependent measurements (Fig. 3). For this study we primarily use 6 eV laser-based ARPES with ~10 μm spatial resolution. Raw spectra are divided by the Fermi-Dirac function convolved with the energy resolution. This analysis shows the band dispersion above E_F within a limited energy range. Below 100 K, α and β bands can be distinguished (Fig. 3, A to D). Above 100 K, the two bands seemingly merge into a hole pocket with the band top ~10 meV above E_F (Fig. 3F). Our observations do not exclude the possibility that the broadening of the α and β bands at high temperatures leads to the appearance of "merging", yet they remain as separate bands throughout the measurement temperature range. Additional Helium-lamp-based ARPES measurements indicate that the band structure near E_F should be best interpreted as intercepting electron and hole bands (fig. S6). Near the Fermi crossings of the electron and hole bands, dramatic band flattening appears at low temperatures (Fig. 3G). In Fig. 3K, we plot the temperature-dependent spectral weight of the α feature, integrated in the range of $[-50, 0]$ meV, after subtracting the incoherent background modeled by a Fermi-Dirac function. In addition, we plot the spectral height of the α feature after subtracting the Fermi-Dirac background. Both quantities scale linearly with $-\log(T)$, where T is the temperature. The pronounced temperature dependence of both the flat band spectral weight and the charge order (fig. S7) suggests that these phenomena do not originate from the structural $\sqrt{3}\times\sqrt{3}$ order observed by x-ray scattering (*44*), which exhibits only weak temperature dependence.

These observations allow us to examine various theoretical scenarios for the formation of the flat band. First, strong electron-phonon coupling can lead to renormalized band dispersions near E_F. The extreme case is the formation of polarons, which give rise to peak-dip-hump features with the dip energy close to the phonon energy (*45*–*47*). Under this scenario, we may associate the spectral dip between α and β (Fig. 3A) with phonons near 15 meV (*48*, *49*). However, such a modification of the single-particle spectral function near E_F should conserve the integrated spectral weight (fig. S8), which is not the case in our results when integrating the background-subtracted spectral weight in the range of either $[-50, 0]$ meV (Fig. 3K) or $[-230, 80]$ meV (fig. S9E). In addition, even with an artificially high electron-phonon coupling constant of $\lambda = 1.0$, the polaronic band structure (fig. S8) still does not yield the extremely flat band α (Fig. 2D), rendering this scenario unlikely. Another possibility is the formation of excitonic band structure, given that the $\sqrt{3}\times\sqrt{3}$ charge order folds an electron pocket from $\overline{K}$ to $\overline{\Gamma}$ to hybridize with the hole pocket at $\overline{\Gamma}$. In the weak-coupling limit, the lower branch of the hybridized band appears in an "M" shape, but in the strong-coupling limit it can have a flat top (fig. S10) (*21*, *50*–*51*). However, this scenario does not explain the formation of the flat band also near the K′ point (Fig. 2D). In addition, Fe_5GeTe_2 is metallic (*31*) where excitonic instabilities should in general be screened. We also considered, through density functional theory plus dynamical mean-field theory (DFT + DMFT) calculations, a scenario where spin-dependent scattering leads to flat dispersions near E_F (fig. S11). However, the calculations do not reproduce the experimentally observed $\log(T)$ spectral-weight evolution (Fig. 3K), nor do they capture the monotonic temperature dependence of the linewidth (fig. S9D). Therefore, the Kondo-like description discussed below should be viewed as phenomenological rather than as a quantitative conclusion directly established by DFT + DMFT. Motivated by the previous STM study (*36*), we thus consider a phenomenological Kondo-like mechanism. The $\log(T)$ scaling of the coherent spectral weight and of the spectral height is consistent with the Kondo-like mechanism (*52*, *53*). In this Kondo-like picture, as temperature increases there is a spectral weight redistribution from the Kondo resonance peak at E_F to the lower and upper Hubbard bands, which are characterized by the energy scale of the Hubbard U (*54*) and is likely out of

Downloaded from https://www.science.org on October 20, 2026

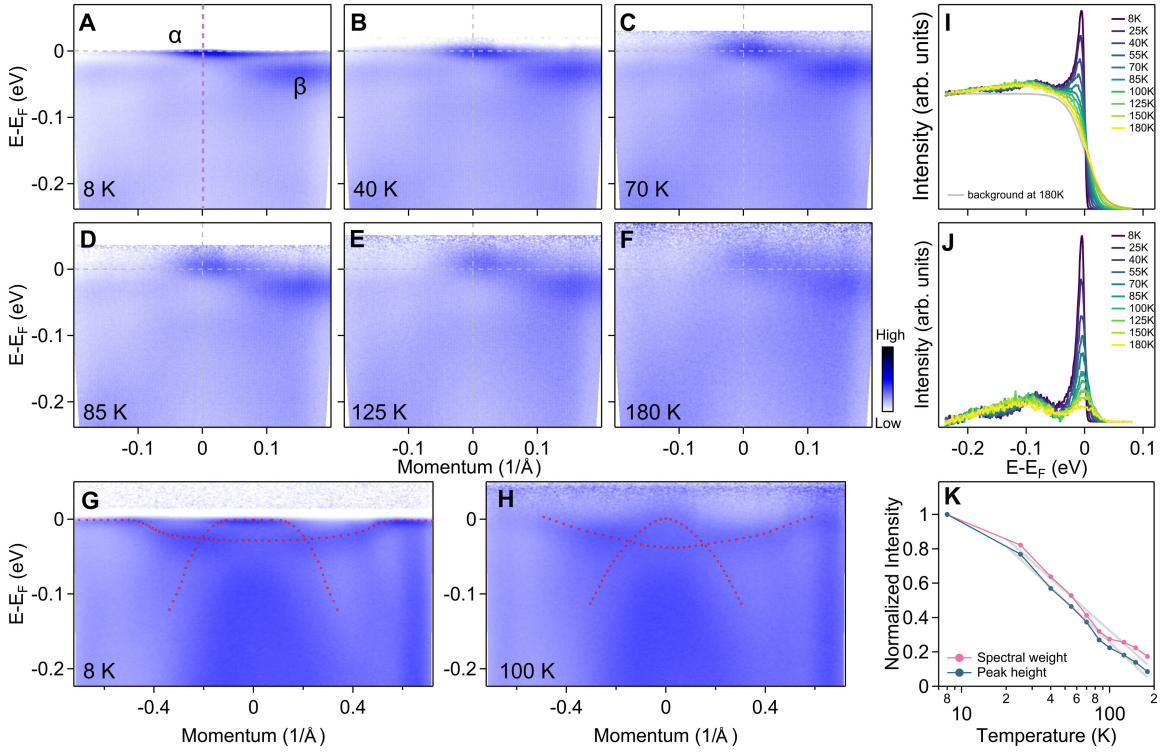


Fig. 3. Temperature-dependent flat band in the UUU phase of Fe_5GeTe_2. (**A** to **F**) ARPES spectra along $\bar{\Gamma} - \bar{M}$ at various temperatures from 8 K to 180 K, taken with a 6 eV *p*-polarized laser. (**G** and **H**) ARPES spectra along $\bar{\Gamma} - \bar{M}$ at 8 K (G) and 180 K (H), acquired with 21.2 eV photons. All spectra in (A to H) are divided by the Fermi-Dirac function convolved with the energy resolution. (**I**) Temperature-dependent energy-distribution curves (EDCs) at $\bar{\Gamma}$, showing the formation of the coherent peak. No Fermi-Dirac division is applied here. (**J**) EDCs from (I) after subtraction of a Fermi-Dirac distribution background. The 180 K background used for the subtraction is indicated by the grey line in (I). (**K**) Temperature dependence of the spectral weight (pink dotted line) and coherent-peak height (blue dotted line) extracted from (J) and normalized to their values at 8 K. The grey lines in (K) are linear fits of the data as a function of log(T). The spectral weight is obtained by integrating the EDCs from −0.05 to 0 eV.

our data acquisition window. Moreover, the temperature-dependent full width at half maximum (FWHM) of the α band agrees with the theoretically predicted linewidth of an effective Kondo resonance peak (fig. S9D), $w(T) = 2\sqrt{(\pi k_B T)^2 + 2(k_B T_K)^2}$, where T and T_K are the sample temperature and the single-ion Kondo temperature; k_B is the Boltzmann constant (*55*–*57*). However, this comparison does not allow us to accurately determine T_K, as the theory-experiment agreement is not obviously better for any specific T_K value (fig. S9D). Our experimental linewidth determined from ARPES is overall smaller than that reported by fitting the Fano line shape in STM in the comparable temperature range (*36*). We speculate that this is because STM probes the momentum-integrated density of states, while micro-ARPES allows us to focus on a small momentum region which helps exclude contributions from other momentum regions without pronounced flat bands.

DISCUSSION

The interaction-driven flat band in Fe_5GeTe_2 is highly intriguing. Even though Kondo physics is traditionally associated with *f*-electrons, Kondo-like systems with *d*-electrons have been identified, such as Fe_3GeTe_2 (*58*) and YFe_2Ge_2 (*59*). A fundamental conceptual difficulty is how the extended *d*-electron wavefunctions enable Kondo-like interactions. It was argued by Xu *et al.* (*59*) that the kinetic frustration, band hybridization, and electronic correlations for *d*-electrons can lead to quasi-localized states, which play the role of the localized states in *f*-electron systems. One should note that such a scenario is by no means equivalent to traditional Kondo lattices, as the coherent quasiparticle peak and hybridization gap do not vanish entirely above the coherence temperature (T^*) (*59*). The *d*-electrons are also not fully localized at high temperatures, but rather exhibit a coherent-to-incoherent crossover as shown in our Fig. 3. Such a coherent-to-incoherent crossover can emerge from a generic Hubbard model with a high coordinate number, where no explicit localized state is required but a heavily renormalized Fermi-liquid-like state emerges due to strong correlation effect (*54*, *60*–*70*). However, the observable quantities, such as extremely flattened band dispersions at E_F, can be effectively described by a Kondo-like interaction, which was shown theoretically (*54*). It is worth pointing out that the charge order can provide a degenerate localized state which helps facilitating the Kondo-like behavior. Lacking a standard terminology to describe this strong correlation effect, the word "Kondo" here is used to only represent the interaction-driven flat band exhibiting temperature scaling.

The discovery of interaction-driven, phenomenological Kondo-like flat bands helps us understand unusual characteristics of Fe_5GeTe_2 by electrical transport and magnetism measurements. A number of resistivity measurements on Fe_5GeTe_2 reported a rapid downturn when the temperature is lowered below 100 K (*30*, *31*, *35*). While these measurements were likely conducted on samples with mixed phases, such resistivity drops are characteristic of Kondo lattices

Downloaded from https://www.science.org on October 20, 2026

where coherent interactions between localized and itinerant bands lead to suppressed resistivity (*71*). A recent study on the flat-band phase of Fe_5GeTe_2 reported the emergence of a Fermi-liquid-like behavior in the low-temperature resistivity, which reinforces this Kondo-like picture (*42*). A polarized neutron scattering experiment showed that the Fe (1) atoms become magnetically ordered below 100 K in the site-disordered phase (*41*), which is inconsistent with Kondo-like behaviors. As we discussed before, the site-disordered phase should be distinguished from our Phase II which is likely associated with the "UUU" configuration of the Fe (1) atoms (*36*). At this stage, it is still challenging to directly compare the surface-sensitive STM (*36*) and micro-ARPES measurements with bulk-sensitive electron (*32*) and x-ray (*44*) diffraction experiments. The diffraction experiments integrate signals from multiple structural phases distributed both in-plane and out-of-plane. The $\sqrt{3} \times \sqrt{3}$ order resolved by these measurements is weakly temperature dependent and predominantly reflects the structural order in the UDD or DUU phase. On the other hand, resonant inelastic x-ray scattering measurement at the Fe L_3-edge revealed a dual character of magnetic excitations in Fe_5GeTe_2 (*44*): spin waves originating from localized spins and magnetic continuum from spin-spin interactions of itinerant electrons, which may suggest a Kondo-like contribution. To understand the phase and strain distribution in the bulk of the Kondo-like Phase II, one future avenue is to fabricate a phase-pure, few-layer-thick Fe_5GeTe_2 flake and perform spatially-resolved electron and x-ray diffraction measurements.

We evaluate the impact of the flat band on the tendency for Fermi surface nesting by calculating the static Lindhard response function (*43*)

$$\chi(\mathbf{q}) = \int \frac{d\mathbf{k}}{(2\pi)^d} \frac{f_{\mathbf{k}} - f_{\mathbf{k+q}}}{\epsilon_{\mathbf{k}} - \epsilon_{\mathbf{k+q}}} \quad (1)$$

where $\mathbf{k}$ and $\mathbf{k} + \mathbf{q}$ represent the initial and final momenta, $\epsilon_{\mathbf{k}}$ is the band dispersion, and f is the Fermi-Dirac function. For a 2D Fermi surface associated with a dispersive band dispersion, $\chi(\mathbf{q})$ is maximized along the direction where the nesting vector connects parallel segments of the Fermi surface (Fig. 4A). However, from our experimentally resolved Fermi surfaces (Fig. 2A) this criterion does not lead to nesting along $\overline{\Gamma} - \overline{K}$. On the other hand, with the flat bands present at $\overline{\Gamma}$ and $\overline{K}$, $\chi(\mathbf{q})$ is maximally enhanced with the nesting vector connecting $\overline{\Gamma}$ and $\overline{K}$, leading to the observed $\sqrt{3} \times \sqrt{3}R30°$ charge order (Fig. 4B). Another scenario is to start with a flat band near $\overline{\Gamma}$ and a dispersive electron-like band near $\overline{K}$ (Fig. 4C), and the $\sqrt{3} \times \sqrt{3}R30°$ charge order folds the quasi-flat band from $\overline{\Gamma}$ to $\overline{K}$. Such a configuration also leads to maximally enhanced $\chi(\mathbf{q})$ along $\overline{\Gamma} - \overline{K}$ (Fig. 4C). Therefore, the flat band at E_F plays a pivotal role in driving the electronic ordering in Phase II of Fe_5GeTe_2. This also explains why the band folding is restricted to 30 meV below E_F (Fig. 1, H and I), where the flat bands reside. We note that this Lindhard-response analysis is based on simplified low-energy band models constructed to capture the experimentally observed Fermi-surface topology and flat-band configurations. It should therefore be viewed as illustrating a plausible nesting-driven instability rather than providing a full ab initio derivation of the charge order.

Importantly, besides Fermi surface nesting, we also evaluate structural instability (*72*), electron-phonon coupling (*24*, *73*), and orbital ordering (*74*) as possible contributors to the charge order. These mechanisms typically involve a spatially modulated lattice distortion, through superstructure modulation, phonon frequency softening or Jahn-Teller-type interactions. The lattice modulation was not observed in the STM measurement on the UUU phase (*36*) and inconsistent with electronic structure reconstruction only in the vicinity of E_F, rendering these scenarios not the driving force for our observed charge order in Fe_5GeTe_2.

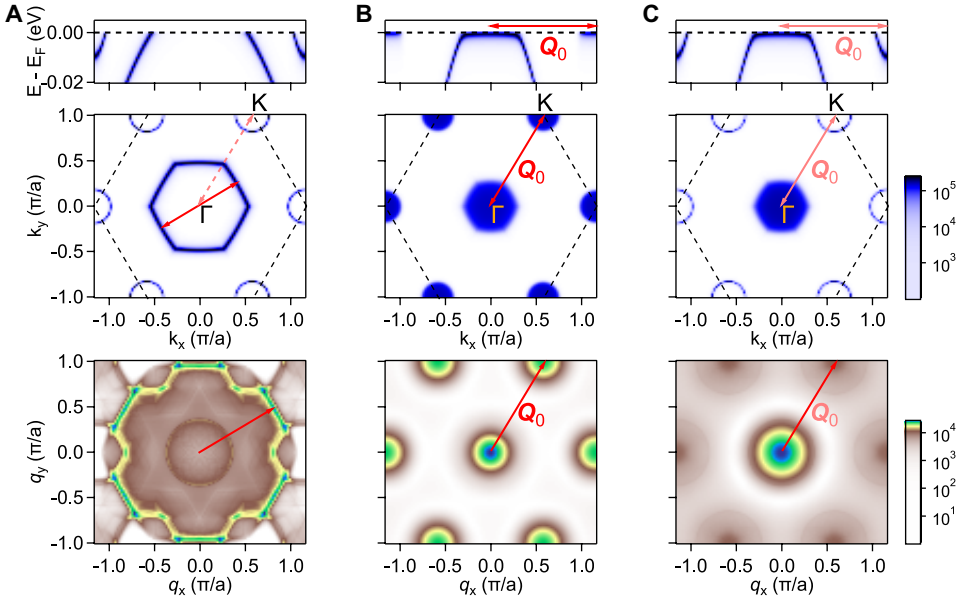


Fig. 4. Theoretical picture of flat-band-induced nesting in Fe_5GeTe_2. (**A**) Simulated static Lindhard response function $\chi(\mathbf{q})$ (bottom) for a simplified dispersive band structure (top), with the corresponding Fermi surface map (middle) showing a hole pocket near $\overline{\Gamma}$ and an electron pocket near $\overline{K}$. This simulation shows preferred nesting vectors that connect the 2 opposite sides of the hole pocket at $\overline{\Gamma}$. (**B**) A similar simulation with flat bands near E_F at $\overline{\Gamma}$ and $\overline{K}$. (**C**) A similar simulation with a flat band near E_F at $\overline{\Gamma}$ and a dispersive electron pocket near $\overline{K}$.

Downloaded from https://www.science.org on October 20, 2026

In summary, we reveal a distinct phase of Fe_5GeTe_2 in which a flat band is formed at E_F and drives a $\sqrt{3} \times \sqrt{3}R30°$ charge order. Clear signatures of the band folding within 30 meV below E_F are observed by high-resolution ARPES, coinciding with the energy range where the flat band resides. Taken together with our calculations of the Lindhard response function, our results suggest Fe_5GeTe_2 as a model system where the interaction-driven flat band directly drives the electronic order. Such a flat band may arise from phenomenological Kondo-like interactions. More interestingly, the intrinsic magnetism in Fe_5GeTe_2 suggests that the time-reversal symmetry is spontaneously broken, leading to the theoretical possibility to realize Chern bands and topological phases (*16*). This highlights the general impact of our observations for low-energy electronic order engineering, and a pressing need to combine micro-device fabrication and low-temperature transport to probe the topological electronic properties.

MATERIALS AND METHODS

Sample growth

Single crystals were grown via iodine-assisted chemical vapor transport following previous methods (*31*). Fe powder, Ge powder, and Te powder were weighed in the molar ratio of 5:1:2, mixed, and placed within a quartz tube along with 2.5 mg/cm^3 of I_2 pieces. The tube was then sealed under a low-pressure Ar atmosphere, and the sealed tubes were placed in a horizontal furnace using the natural temperature gradient with the source material at the center of the furnace. The furnace was ramped to 760°C in 12 hours, dwelled for 2 weeks, and then slowly cooled to room temperature for slow-cooling crystals. Some crystals were subsequently re-sealed in a quartz tube under vacuum, placed in a furnace at 750 K for two hours, and quenched in ice water to get quenched crystals. We could also create a quenched sample by heating it for 20 minutes on a hot plate at 573 K, and quenching it by thermal contact with a metal kept at 77 K.

ARPES measurements

The high-resolution ARPES measurements were performed on a Multi-Resolution Photoemission Spectroscopy platform at the University of Chicago (*75*). The 6 eV laser was generated by frequency quadrupling of a Ti:Sapphire oscillator with an 80 MHz repetition rate. The 6 eV laser spot size is 10×15 μm^2 (FWHM) and incident on the sample at ≈45°. The analyzer slit is perpendicular to the plane defined by the laser propagation direction and the sample normal. The energy resolution of the 6 eV laser ARPES is 4 meV. The 21.2 eV ARPES measurements were carried out by using a helium discharge lamp (Scienta VUV5000) with an energy resolution of 6 meV.

DFT + DMFT calculations

DFT + DMFT calculations were performed using Rutgers DFT + Embedded DMFT (eDMFT) functional code (*76*). The correlation effect of Fe 3*d* orbitals is treated by a DMFT loop on top of an effective one-electron Hamiltonian obtained from the WIEN2k calculation, which employs the full-potential augmented plane wave method (*77*). Due to the computational cost, we modeled a Fe_5GeTe_2 monolayer for the calculations, rather than the bulk structure which contains three layers per unit cell due to stacking. The five inequivalent Fe sites within the structure were treated as five different impurity problems within the DMFT framework. A local DMFT basis was constructed by diagonalizing the hybridization matrix at zero frequency in the real-harmonic representation. The hybridization energy window, spanning from −10 to 10 eV with respect to the Fermi level, was adopted for the charge self-consistent calculations. The interaction parameters were chosen as $U = 5$ eV and $J = 0.8$ eV, and the nominal double-counting correction was adopted. The impurity problem was solved using continuous-time quantum Monte Carlo (CTQMC) method (*78*).

Supplementary Materials

This PDF file includes:

Supplementary Text
Figs. S1 to S11
References

REFERENCES

1. Y. Jiang, X. Lai, K. Watanabe, T. Taniguchi, K. Haule, J. Mao, E. Y. Andrei, Charge order and broken rotational symmetry in magic-angle twisted bilayer graphene. *Nature* **573**, 91–95 (2019).
2. Y. Cao, V. Fatemi, S. Fang, K. Watanabe, T. Taniguchi, E. Kaxiras, P. Jarillo-Herrero, Unconventional superconductivity in magic-angle graphene superlattices. *Nature* **556**, 43–50 (2018).
3. H. Tian, X. Gao, Y. Zhang, S. Che, T. Xu, P. Cheung, K. Watanabe, T. Taniguchi, M. Randeria, F. Zhang, C. N. Lau, M. W. Bockrath, Evidence for Dirac flat band superconductivity enabled by quantum geometry. *Nature* **614**, 440–444 (2023).
4. Y. Cao, V. Fatemi, A. Demir, S. Fang, S. L. Tomarken, J. Y. Luo, J. D. S. Yamagishi, K. Watanabe, T. Taniguchi, E. Kaxiras, R. C. Ashoori, P. Jarillo-Herrero, Correlated insulator behaviour at half-filling in magic-angle graphene superlattices. *Nature* **556**, 80–84 (2018).
5. M. Serlin, C. L. Tschirhart, H. Polshyn, Y. Zhang, J. Zhu, K. Watanabe, T. Taniguchi, L. Balents, A. F. Young, Intrinsic quantized anomalous Hall effect in a moiré heterostructure. *Science* **367**, 900–903 (2020).
6. J. Cai, E. Anderson, C. Wang, X. Zhang, X. Liu, W. Holtzmann, Y. Zhang, F. Fan, T. Taniguchi, K. Watanabe, Y. Ran, T. Cao, L. Fu, D. Xiao, W. Yao, X. Xu, Signatures of fractional quantum anomalous Hall states in twisted $MoTe_2$. *Nature* **622**, 63–68 (2023).
7. Y. Zeng, Z. Xia, K. Kang, J. Zhu, P. Knüppel, C. Vaswani, K. Watanabe, T. Taniguchi, K. F. Mak, J. Shan, Thermodynamic evidence of fractional Chern insulator in moiré $MoTe_2$. *Nature* **622**, 69–73 (2023).
8. Z. Lu, T. Han, Y. Yao, A. P. Reddy, J. Yang, J. Seo, K. Watanabe, T. Taniguchi, L. Fu, L. Ju, Fractional quantum anomalous Hall effect in multilayer graphene. *Nature* **626**, 759–764 (2024).
9. E. H. Lieb, Two theorems on the Hubbard model. *Phys. Rev. Lett.* **62**, 1201–1204 (1989).
10. M. R. Slot, T. S. Gardenier, P. H. Jacobse, G. C. P. van Miert, S. N. Kempkes, S. J. M. Zevenhuizen, C. M. Smith, D. Vanmaekelbergh, I. Swart, Experimental realization and characterization of an electronic Lieb lattice. *Nat. Phys.* **13**, 672–676 (2017).
11. H. M. Guo, M. Franz, Topological insulator on the kagome lattice. *Phys. Rev. B* **80**, 113102 (2009).
12. M. Kang, L. Ye, S. Fang, J. S. You, A. Levitan, M. Han, J. I. Facio, C. Jozwiak, A. Bostwick, E. Rotenberg, M. K. Chan, R. D. McDonald, D. Graf, K. Kaznatcheev, E. Vescovo, D. C. Bell, E. Kaxiras, J. van den Brink, M. Richter, M. P. Ghimire, J. G. Checkelsky, R. Comin, Dirac fermions and flat bands in the ideal kagome metal FeSn. *Nat. Mater.* **19**, 163–169 (2020).
13. X. Teng, J. S. Oh, H. Tan, L. Chen, J. Huang, B. Gao, J. X. Yin, J. H. Chu, M. Hashimoto, D. Lu, C. Jozwiak, A. Bostwick, E. Rotenberg, G. E. Granroth, B. Yan, R. J. Birgeneau, P. Dai, M. Yi, Magnetism and charge density wave order in kagome FeGe. *Nat. Phys.* **19**, 814–822 (2023).
14. A. Nag, Y. Peng, J. Li, S. Agrestini, H. C. Robarts, M. García-Fernández, A. C. Walters, Q. Wang, Q. Yin, H. Lei, Z. Yin, K.-J. Zhou, Correlation driven near-flat band Stoner excitations in a Kagome magnet. *Nat. Commun.* **13**, 7317 (2022).
15. Z. Wang, Y. Guo, H. Y. Huang, F. Xie, Y. Huang, B. Gao, J. S. Oh, H. Wu, J. Okamoto, G. Channagowdra, C. T. Chen, F. Ye, X. Lu, Z. Liu, Z. Ren, Y. Fang, Y. Wang, A. Biswas, Y. Zhang, Z. Yue, C. Hu, C. Jozwiak, A. Bostwick, E. Rotenberg, M. Hashimoto, D. Lu, J. Kono, J. H. Chu, B. I. Yakobson, R. J. Birgeneau, G. H. Cao, A. Fujimori, D. J. Huang, Q. Si, M. Yi, P. Dai, Spin excitations and flat electronic bands in a Cr-based kagome superconductor. *Nat. Commun.* **16**, 7573 (2025).
16. L. Chen, F. Xie, S. Sur, H. Hu, S. Paschen, J. Cano, Q. Si, Emergent flat band and topological Kondo semimetal driven by orbital-selective correlations. *Nat. Commun.* **15**, 5242 (2024).
17. J. G. Checkelsky, B. A. Bernevig, P. Coleman, Q. Si, S. Paschen, Flat bands, strange metals and the Kondo effect. *Nat. Rev. Mater.* **9**, 509–526 (2024).
18. W. Zhao, B. Shen, Z. Tao, S. Kim, P. Knüppel, Z. Han, Y. Zhang, K. Watanabe, T. Taniguchi, D. Chowdhury, J. Shan, K. F. Mak, Emergence of ferromagnetism at the onset of moiré Kondo breakdown. *Nat. Phys.* **20**, 1772–1777 (2024).

Downloaded from https://www.science.org on October 20, 2026

19. J. A. Sobota, Y. He, Z. X. Shen, Angle-resolved photoemission studies of quantum materials. *Rev. Mod. Phys.* **93**, 025006 (2021).
20. Y. Choi, H. Kim, C. Lewandowski, Y. Peng, A. Thomson, R. Polski, Y. Zhang, K. Watanabe, T. Taniguchi, J. Alicea, S. Nadj-Perge, Interaction-driven band flattening and correlated phases in twisted bilayer graphene. *Nat. Phys.* **17**, 1375–1381 (2021).
21. Y. D. Wang, W. L. Yao, Z. M. Xin, T. T. Han, Z. G. Wang, L. Chen, C. Cai, Y. Li, Y. Zhang, Band insulator to Mott insulator transition in 1*T*-TaS_2. *Nat. Commun.* **11**, 4215 (2020).
22. J. A. Wilson, F. J. Di Salvo, S. Mahajan, Charge-density waves in metallic, layered, transition-metal dichalcogenides. *Phys. Rev. Lett.* **32**, 882–885 (1974).
23. K. Rossnagel, On the origin of charge-density waves in select layered transition-metal dichalcogenides. *J. Phys. Condens. Matter* **23**, 213001 (2011).
24. F. Weber, S. Rosenkranz, J.-P. Castellan, R. Osborn, R. Hott, R. Heid, K.-P. Bohnen, T. Egami, A. H. Said, D. Reznik, Extended phonon collapse and the origin of the charge-density wave in 2H-$NbSe_2$. *Phys. Rev. Lett.* **107**, 107403 (2011).
25. T. Ritschel, J. Trinckauf, K. Koepernik, B. Büchner, M. v. Zimmermann, H. Berger, Y. I. Joe, P. Abbamonte, J. Geck, Orbital textures and charge density waves in transition metal dichalcogenides. *Nat. Phys.* **11**, 328–331 (2015).
26. B. R. Ortiz, L. C. Gomes, J. R. Morey, M. Winiarski, M. Bordelon, J. S. Mangum, I. W. H. Oswald, J. A. Rodriguez-Rivera, J. R. Neilson, S. D. Wilson, E. Ertekin, T. M. McQueen, E. S. Toberer, New kagome prototype materials: discovery of KV_3Sb_5, RbV_3Sb_5, and CsV_3Sb_5. *Phys. Rev. Mater.* **3**, 094407 (2019).
27. Y.-X. Jiang, J.-X. Yin, M. M. Denner, N. Shumiya, B. R. Ortiz, G. Xu, Z. Guguchia, J. He, M. S. Hossain, X. Liu, J. Ruff, L. Kautzsch, S. S. Zhang, G. Chang, I. Belopolski, Q. Zhang, T. A. Cochran, D. Multer, M. Litskevich, Z.-J. Cheng, X. P. Yang, Z. Wang, R. Thomale, T. Neupert, S. D. Wilson, M. Z. Hasan, Unconventional chiral charge order in kagome superconductor KV_3Sb_5. *Nat. Mater.* **20**, 1353–1357 (2021).
28. C. Mielke III, D. Das, J.-X. Yin, H. Liu, R. Gupta, Y.-X. Jiang, M. Medarde, X. Wu, H. C. Lei, J. J. Chang, P. Dai, Q. Si, H. Miao, R. Thomale, T. Neupert, Y. Shi, R. Khasanov, M. Z. Hasan, H. Luetkens, Z. Guguchia, Time-reversal symmetry-breaking charge order in a kagome superconductor. *Nature* **602**, 245–250 (2022).
29. H. Lin, C. L. Jacobs, C. Yan, G. M. Nolan, G. Berruto, P. Singleton, K. D. Nguyen, Y. Bai, Q. Gao, X. Wu, C. X. Liu, G. Yan, S. Choi, C. Liu, N. P. Guisinger, P. Y. Huang, S. Mandal, S. Yang, A topological superconductor tuned by electronic correlations. *Nat. Commun.* **17**, 1188 (2026).
30. A. F. May, D. Ovchinnikov, Q. Zheng, R. Hermann, S. Calder, B. Huang, Z. Fei, Y. Liu, X. Xu, M. A. McGuire, Ferromagnetism near room temperature in the cleavable van der Waals crystal Fe_5GeTe_2. *ACS Nano* **13**, 4436–4442 (2019).
31. A. F. May, C. A. Bridges, M. A. McGuire, Physical properties and thermal stability of $Fe_{5-x}GeTe_2$ single crystals. *Phys. Rev. Mater.* **3**, 104401 (2019).
32. Y. Gao, Q. Yin, Q. Wang, Z. Li, J. Cai, T. Zhao, H. Lei, S. Wang, Y. Zhang, B. Shen, Spontaneous (Anti)meron chains in the domain walls of van der Waals ferromagnetic $Fe_{5-x}GeTe_2$. *Adv. Mater.* **32**, e2005228 (2020).
33. T. T. Ly, J. Park, K. Kim, H. B. Ahn, N. J. Lee, K. Kim, T. E. Park, G. Duvjir, N. H. Lam, K. Jang, C. Y. You, Y. Jo, S. K. Kim, C. Lee, S. Kim, J. Kim, Direct observation of Fe-Ge ordering in $Fe_{5-x}GeTe_2$ crystals and resultant helimagnetism. *Adv. Funct. Mater.* **31**, 2009758 (2021).
34. S. Ershadrad, S. Ghosh, D. Wang, Y. Kvashnim, B. Sanyal, Unusual magnetic features in two-dimensional Fe_5GeTe_2 induced by structural reconstructions. *J. Phys. Chem. Lett.* **13**, 4877–4883 (2022).
35. H. Wu, L. Chen, P. Malinowski, B. G. Jang, Q. Deng, K. Scott, J. Huang, J. P. C. Ruff, Y. He, X. Chen, C. Hu, Z. Yue, J. S. Oh, X. Teng, Y. Guo, M. Klemm, C. Shi, Y. Shi, C. Setty, T. Werner, M. Hashimoto, D. Lu, T. Yilmaz, E. Vescovo, S. K. Mo, A. Fedorov, J. D. Denlinger, Y. Xie, B. Gao, J. Kono, P. Dai, Y. Han, X. Xu, R. J. Birgeneau, J. X. Zhu, E. H. da Silva Neto, L. Wu, J. H. Chu, Q. Si, M. Yi, Reversible non-volatile electronic switching in a near-room-temperature van der Waals ferromagnet. *Nat. Commun.* **15**, 2739 (2024).
36. P. P. R. Luo, H. C. Hsu, L. S. Lin, H. Y. Chen, X. Y. Xie, C. N. Kuo, J. P. Chou, C. S. Lue, Y. P. Chiu, Direct evidence of coupling between charge density wave and Kondo lattice in ferromagnet Fe_5GeTe_2. *Nat. Commun.* **16**, 5080 (2025).
37. K. Yamagami, Y. Fujisawa, B. Driesen, C. H. Hsu, K. Kawaguchi, H. Tanaka, T. Kondo, Y. Zhang, H. Wadati, K. Araki, T. Takeda, Y. Takeda, T. Muro, F. C. Chuang, Y. Niimi, K. Kuroda, M. Kobayashi, Y. Okada, Itinerant ferromagnetism mediated by giant spin polarization of the metallic ligand band in the van der Waals magnet Fe_5GeTe_2. *Phys. Rev. B* **103**, L060403 (2021).
38. X. Wu, L. Lei, Q. Yin, N. N. Zhao, M. Li, Z. Wang, Q. Liu, W. Song, H. Ma, P. Ding, Z. Cheng, K. Liu, H. Lei, S. Wang, Direct observation of competition between charge order and itinerant ferromagnetism in the van der Waals crystal $Fe_{5-x}GeTe_2$. *Phys. Rev. B* **104**, 165101 (2021).
39. K. Huang, Z. Li, D. Guo, H. Yang, Y. Li, A. Liang, F. Wu, L. Xu, L. Yang, W. Ji, Y. Guo, Y. Chen, Z. Liu, Measurement of electronic structure in van der Waals ferromagnet $Fe_{5-x}GeTe_2$. *Chin. Phys. B* **31**, 057404 (2022).
40. Z. Li, D. Guo, K. Huang, G. Ma, X. Liu, Y. Wu, J. Yuan, Z. Tao, B. Wang, X. Wang, Z. Zou, N. Yu, G. Yu, J. Xue, Z. Liu, W. Ji, J. Li, Y. Guo, Robust weak antilocalization effect up to ~120 K in the van der Waals crystal $Fe_{5-x}GeTe_2$ with near-room-temperature ferromagnetism. *J. Phys. Chem. Lett.* **14**, 5456–5465 (2023).
41. H. Wu, J. Huang, C. Hu, L. Chen, Y. Hao, Y. Shi, P. Malinowski, Y. Guo, B. G. Jang, J. X. Zhu, A. F. May, T. Werner, S. Wang, X. Chen, Y. Xie, B. Gao, Y. Zhang, Z. Yue, Z. Ren, M. Hashimoto, D. Lu, A. Fedorov, S. K. Mo, J. Kono, Y. He, R. J. Birgeneau, P. Dai, X. Xu, H. Cao, Q. Si, J. H. Chu, M. Yi, Dichotomy of flat bands in the van der Waals ferromagnet Fe_5GeTe_2. *Phys. Rev. B* **113**, 125120 (2026).
42. S. Huh, K. Kawaguchi, M. Haze, Y. Hasegawa, Y. Dong, K. Aido, A. Harasawa, B. R. M. Smith, K. Yamagami, Y. Fujisawa, C. H. Hsu, K. Kuroda, H. J. Shin, J. Y. Seo, N. Lee, Y. J. Choi, Y. Kinoshita, M. Tokunaga, M. Hashimoto, D. Lu, Y. Okada, T. Kondo, Observation of a d-orbital flat band near the Fermi level realizing a Kondo lattice in a van der Waals material. *Commun. Mater.* **7**, 23 (2026).
43. G. Grüner, Density waves in solids (Perseus Publishing, Cambridge, MA, 1994).
44. V. K. Bhartiya, T. Kim, J. Li, T. P. Darlington, D. J. Rizzo, Y. Gu, S. Fan, C. Nelson, J. W. Freeland, X. Xu, D. N. Basov, J. Pelliciari, A. F. May, C. Mazzoli, V. Bisogni, Magnetic excitations and absence of charge order in the van der Waals ferromagnet $Fe_{4.75}GeTe_2$. *npj Quantum Mater.* **10**, 80 (2025).
45. Z. K. Liu, R. H. He, D. H. Lu, M. Yi, Y. L. Chen, M. Hashimoto, R. G. Moore, S. K. Mo, E. A. Nowadnick, J. Hu, T. J. Liu, Z. Q. Mao, T. P. Devereaux, Z. Hussain, Z. X. Shen, Measurement of coherent polarons in the strongly coupled antiferromagnetically ordered iron-chalcogenide $Fe_{1.02}Te$ using angle-resolved photoemission spectroscopy. *Phys. Rev. Lett.* **110**, 037003 (2013).
46. N. Mannella, W. L. Yang, K. Tanaka, X. J. Zhou, H. Zheng, J. F. Mitchell, J. Zaanen, T. P. Devereaux, N. Nagaosa, Z. Hussain, Z. X. Shen, Polaron coherence condensation as the mechanism for colossal magnetoresistance in layered manganites. *Phys. Rev. B* **76**, 233102 (2007).
47. L. Perfetti, S. Mitrovic, G. Margaritondo, M. Grioni, L. Forró, L. Degiorgi, H. Höchst, Mobile small polarons and the Peierls transition in the quasi-one-dimensional conductor $K_{0.3}MoO_3$. *Phys. Rev. B* **66**, 075107 (2002).
48. R. L. Yadav, P. Bag, C. C. Lai, Y. K. Kuo, C. N. Kuo, C. S. Lue, Thermal history-dependent characteristics in van der Waals ferromagnet $Fe_{5-x}GeTe_2$ (x≈0.16). *APL Mater.* **12**, 081103 (2024).
49. H. Yu, X. Li, Y. Q. Bie, L. Yan, L. Zhou, P. Yu, G. Yang, Quantum metric third-order nonlinear Hall effect in a non-centrosymmetric ferromagnet. *Nat. Commun.* **16**, 7698 (2025).
50. H. Cercellier, C. Monney, F. Clerc, C. Battaglia, L. Despont, M. G. Garnier, H. Beck, P. Aebi, L. Patthey, H. Berger, L. Forró, Evidence for an excitonic insulator phase in 1*T*-$TiSe_2$. *Phys. Rev. Lett.* **99**, 146403 (2007).
51. Y. Wakisaka, T. Sudayama, K. Takubo, T. Mizokawa, M. Arita, H. Namatame, M. Taniguchi, N. Katayama, M. Nohara, H. Takagi, Excitonic insulator state in Ta_2NiSe_5 probed by photoemission spectroscopy. *Phys. Rev. Lett.* **103**, 026402 (2009).
52. S. Jang, J. D. Denlinger, J. W. Allen, V. S. Zapf, M. B. Maple, J. N. Kim, B. G. Jang, J. H. Shim, Evolution of the Kondo lattice electronic structure above the transport coherence temperature. *Proc. Natl. Acad. Sci. U.S.A.* **117**, 23467–23476 (2020).
53. Q. Y. Chen, D. F. Xu, X. H. Niu, J. Jiang, R. Peng, H. C. Xu, C. H. P. Wen, Z. F. Ding, K. Huang, L. Shu, Y. J. Zhang, H. Lee, V. N. Strocov, M. Shi, F. Bisti, T. Schmitt, Y. B. Huang, P. Dudin, X. C. Lai, S. Kirchner, H. Q. Yuan, D. L. Feng, Direct observation of how the heavy-fermion state develops in $CeCoIn_5$. *Phys. Rev. B* **96**, 045107 (2017).
54. J. Merino, R. H. McKenzie, Transport properties of strongly correlated metals: A dynamical mean-field approach. *Phys. Rev. B* **61**, 7996–8008 (2000).
55. K. Nagaoka, T. Jamneala, M. Grobis, M. F. Crommie, Temperature dependence of a single Kondo impurity. *Phys. Rev. Lett.* **88**, 077205 (2002).
56. S. Ernst, S. Kirchner, C. Krellner, C. Geibel, G. Zwicknagl, F. Steglich, S. Wirth, Emerging local Kondo screening and spatial coherence in the heavy-fermion metal $YbRh_2Si_2$. *Nature* **474**, 362–366 (2011).
57. F. Reinert, D. Ehm, S. Schmidt, G. Nicolay, S. Hüfner, J. Kroha, O. Trovarelli, C. Geibel, Temperature dependence of the Kondo resonance and its satellites in $CeCu_2Si_2$. *Phys. Rev. Lett.* **87**, 106401 (2001).
58. Y. Zhang, H. Lu, X. Zhu, S. Tan, W. Feng, Q. Liu, W. Zhang, Q. Chen, Y. Liu, X. Luo, D. Xie, L. Luo, Z. Zhang, X. Lai, Emergence of Kondo lattice behavior in a van der Waals itinerant ferromagnet, Fe_3GeTe_2. *Sci. Adv.* **4**, eaao6791 (2018).
59. B. Xu, R. Liu, H. Wo, Z. Liao, S. Yi, C. Li, J. Zhao, X. Qiu, Z. Yin, C. Bernhard, Unraveling the origin of Kondo-like behavior in the 3*d*-electron heavy-fermion compound YFe_2Ge_2. *Proc. Natl. Acad. Sci. U.S.A.* **121**, e2401430121 (2024).
60. T. Valla, P. D. Johnson, Z. Yusof, B. Wells, Q. Li, S. M. Loureiro, R. J. Cava, M. Mikami, Y. Mori, M. Yoshimura, T. Sasaki, Coherence-incoherence and dimensional crossover in layered strongly correlated metals. *Nature* **417**, 627–630 (2002).
61. T. Pruschke, D. L. Cox, M. Jarrell, Hubbard model at infinite dimensions: Thermodynamic and transport properties. *Phys. Rev. B* **47**, 3553–3565 (1993).
62. A. Georges, G. Kotliar, W. Krauth, M. J. Rozenberg, Dynamical mean-field theory of strongly correlated fermion systems and the limit of infinite dimensions. *Rev. Mod. Phys.* **68**, 13–125 (1996).
63. C.-N. Yeh, F. Petocchi, A. Hampel, P. Werner, O. Parcollet, A. Georges, M. Morales, Electronic correlations and dynamical screening with ab initio quantum embedding. *arXiv*:2603.12336 (2026).

Downloaded from https://www.science.org on October 20, 2026

64. F. B. Kugler, J. Lee-Hand, H. LaBollita, L. Van Muñoz, J. Kaye, S. Beck, A. Hampel, A. Georges, C. E. Dreyer, Fermi-liquid T^2 resistivity: Dynamical mean-field theory meets experiment. *Phys. Rev. B* **113**, L081105 (2026).
65. A. Hardy, O. Parcollet, A. Georges, A. A. Patel, Enhanced strange metallicity due to Hubbard-U Coulomb repulsion. *Phys. Rev. Lett.* **134**, 036502 (2025).
66. K. Haule, G. Kotliar, Coherence-incoherence crossover in the normal state of iron oxypnictides and importance of Hund's rule coupling. *New J. Phys.* **11**, 025021 (2009).
67. A. Georges, L. de' Medici, J. Mravlje, Strong correlations from Hund's coupling. *Annu. Rev. Condens. Matter Phys.* **4**, 137–178 (2013).
68. J. Mravlje, M. Aichhorn, T. Miyake, K. Haule, G. Kotliar, A. Georges, Coherence-incoherence crossover and the mass-renormalization puzzles in Sr_2RuO_4. *Phys. Rev. Lett.* **106**, 096401 (2011).
69. X. Deng, K. M. Stadler, K. Haule, A. Weichselbaum, J. von Delft, G. Kotliar, Signatures of Mottness and Hundness in archetypal correlated metals. *Nat. Commun.* **10**, 2721 (2019).
70. K. M. Stadler, G. Kotliar, A. Weichselbaum, J. von Delft, Hundness versus Mottness in a three-band Hubbard–Hund model: On the origin of strong correlations in Hund metals. *Ann. Phys.* **405**, 365–409 (2019).
71. O. Trovarelli, C. Geibel, S. Mederle, C. Langhammer, F. M. Grosche, P. Gegenwart, M. Lang, G. Sparn, F. Steglich, $YbRh_2Si_2$: Pronounced non-Fermi-liquid effects above a low-lying magnetic phase transition. *Phys. Rev. Lett.* **85**, 626–629 (2000).
72. P. D. C. King, J. A. Rosen, W. Meevasana, A. Tamai, E. Rozbicki, R. Comin, G. Levy, D. Fournier, Y. Yoshida, H. Eisaki, K. M. Shen, N. J. C. Ingle, A. Damascelli, F. Baumberger, Structural Origin of Apparent Fermi Surface Pockets in Angle-Resolved Photoemission of $Bi_2Sr_{2-x}La_xCuO_{6+\delta}$. *Phys. Rev. Lett.* **106**, 127005 (2011).
73. X. Shen, R. Heid, R. Hott, A.-A. Haghighirad, B. Salzmann, M. dos Reis Cantarino, C. Monney, A. H. Said, M. Frachet, B. Murphy, K. Rossnagel, S. Rosenkranz, F. Weber, Precursor region with full phonon softening above the charge-density-wave phase transition in 2H-$TaSe_2$. *Nat. Commun.* **14**, 7282 (2023).
74. J. van den Brink, G. Khaliullin, D. Khomskii, Charge and orbital order in half-doped manganites. *Phys. Rev. Lett.* **83**, 5118–5121 (1999).
75. C. Yan, E. Green, R. Fukumori, N. Protic, S. H. Lee, S. Fernandez-Mulligan, R. Raja, R. Erdakos, Z. Mao, S. Yang, An integrated quantum material testbed with multi-resolution photoemission spectroscopy. *Rev. Sci. Instrum.* **92**, 113907 (2021).
76. K. Haule, C.-H. Yee, K. Kim, Dynamical mean-field theory within the full-potential methods: Electronic structure of $CeIrIn_5$, $CeCoIn_5$, and $CeRhIn_5$. *Phys. Rev. B* **81**, 195107 (2010).
77. P. Blaha, K. Schwarz, F. Tran, R. Laskowski, G. K. H. Madsen, L. D. Marks, WIEN2k: An APW+lo program for calculating the properties of solids. *J. Chem. Phys.* **152**, 074101 (2020).
78. K. Haule, Quantum Monte Carlo impurity solver for cluster dynamical mean-field theory and electronic structure calculations with adjustable cluster base. *Phys. Rev. B* **75**, 155113 (2007).
79. G. L. Goodvin, M. Berciu, G. A. Sawatzky, Green's function of the Holstein polaron. *Phys. Rev. B* **74**, 245104 (2006).

Acknowledgments: We thank H. Wu, M. Yi, X. Wang, S. Huang, J. Zhu, and Z. Shen for helpful discussions. **Funding:** This work was supported by: The U.S. Department of Energy DE-SC0022960 (S.Y., Q.G., G.B., K.D.N., H.L.), The U.S. Department of Energy DE-SC0019443 (C.H., X.X., J.C.), The Gordon and Betty Moore Foundation GBMF12763 (P.L., S.Y.), The National Research Council of Science & Technology (NST) grant by the Korea Government (MSIT) CAP25061–000 (B.G.J.), and The National Research Foundation (NRF) of Korea RS-2026-25488595 (B.G.J.). **Author contributions:** Conceptualization: S.Y., P.L., G.B., K.D.N., B.G.J. Supervision: S.Y., P.L., J.C., C.H., Methodology: Q.G., K.D.N., H.L., G.B., B.G. Investigation: Q.G., K.D.N., H.L., G.B., B.G.J., Data curation: Q.G., G.B., K.D.N., B.G.J., B.G. Validation: Q.G., G.B., K.D.N., B.G.J., B.G., X.X. Formal analysis: Q.G., K.D.N., P.L., G.B., B.G.J., B.G. Visualization: Q.G., G.B., K.D.N., B.G.J., B.G. Software: Q.G., K.D.N., H.L., B.G.J., B.G. Resources: P.M., C.H., J.C., X.X., K.D.N., H.L., B.G.J. Writing—original draft: S.Y., Q.G., K.D.N. Writing—review & editing: S.Y., Q.G., G.B., K.D.N., P.L., B.G.J., J.C., B.G., H.L., X.X. Project administration: S.Y., Q.G., X.X., Funding acquisition: S.Y., P.L., J.C., X.X. **Competing interests:** The authors declare that they have no competing interests. **Data, code, and materials availability:** All data and code needed to evaluate and reproduce the results in the paper are present in the paper and/or the Supplementary Materials. This study did not generate materials.

Submitted 19 February 2026
Accepted 6 July 2026
Published 7 August 2026
10.1126/sciadv.aeg5930

Downloaded from https://www.science.org on October 20, 2026

ScienceAdvances

Interaction-driven flat band and charge order in Fe_5GeTe_2

Qiang Gao, Gabriele Berruto, Khanh Duy Nguyen, Chaowei Hu, Paul Malinowski, Haoran Lin, Beomjoon Goh, Bo Gyu Jang, Xiaodong Xu, Peter Littlewood, Jiun-Haw Chu, and Shuolong Yang

Sci. Adv. **12** (32), eaeg5930. DOI: 10.1126/sciadv.aeg5930

View the article online
https://www.science.org/doi/10.1126/sciadv.aeg5930
Permissions
https://www.science.org/help/reprints-and-permissions

Downloaded from https://www.science.org on October 20, 2026

Use of this article is subject to the Terms of service

Science Advances (ISSN 2375-2548) is published by the American Association for the Advancement of Science. 1200 New York Avenue NW, Washington, DC 20005. The title *Science Advances* is a registered trademark of AAAS.

Copyright © 2026 The Authors, some rights reserved; exclusive licensee American Association for the Advancement of Science. No claim to original U.S. Government Works. Distributed under a Creative Commons Attribution NonCommercial License 4.0 (CC BY-NC).